

Numerical modeling of seismicity induced by fluid injection in naturally fractured reservoirs

Xueping Zhao¹ and R. Paul Young²

ABSTRACT

The interaction between hydraulic and natural fractures is of great interest for the energy resource industry because natural fractures can significantly influence the overall geometry and effectiveness of hydraulic fractures. Microseismic monitoring provides a unique tool to monitor the evolution of fracturing around the treated rock reservoir, and seismic source mechanisms can yield information about the nature of deformation. We performed a numerical modeling study using a 2D distinct-element particle flow code (PFC^{2D}) to simulate realistic conditions and increase understanding of fracturing mechanisms in naturally fractured reservoirs, through comparisons with results of the geometry of hydraulic fractures and seismic source information (locations, magnitudes, and me-

chanisms) from both laboratory experiments and field observations. A suite of numerical models with fully dynamic and hydromechanical coupling was used to examine the interaction between natural and induced fractures, the effect of orientation of a preexisting fracture, the influence of differential stress, and the relationship between the fluid front, fracture tip, and induced seismicity. The numerical results qualitatively agree with the laboratory and field observations, and suggest possible mechanics for new fracture development and their interaction with a natural fracture (e.g., a tectonic fault). Therefore, the tested model could help in investigating the potential extent of induced fracturing in naturally fractured reservoirs, and in interpreting microseismic monitoring results to assess the effectiveness of a hydraulic fracturing project.

INTRODUCTION

Microseismic (MS) monitoring is an established technique used to monitor the effectiveness and response to a hydrofracture well simulation intended to improve the production of hydrocarbons from unconventional oil and gas reservoirs (Maxwell and Urbancic, 2001; Young and Baker, 2001; Ramakrishnan et al., 2009), enhance design of geothermal energy extraction in hot dry rock (Norio et al., 2008), and to assure long-term storage of greenhouse gas (Lumley et al., 2008; White, 2009). Due to the ubiquity of natural fractures, the interaction between hydraulic (induced) and natural fractures is of great interest for the energy resource industry because natural fractures can significantly influence the overall geometry and effectiveness of hydraulic fractures.

A considerable amount of research has been carried out in the past few decades trying to understand the complexity and

mechanics of hydraulic fractures in fractured reservoirs. Blanton (1986) conducted scaled laboratory hydrofracturing experiments on naturally fractured Devonian shale and hydrostone. These experiments showed that hydraulic fractures crossed preexisting fractures only under high differential stress and high approaching angles, while at low differential stress and low angles of approach the existing fracture opened, diverting the fracturing fluid and at least temporarily preventing the induced fracture from crossing. Warpinski and Teufel (1987) conducted mineback experiments to study the effect of geological discontinuities on hydraulic fracture propagation. They derived a fracture interaction criterion to predict whether the induced fracture causes a shear slippage on the natural fracture plane, leading to the arrest of the propagating fracture, or whether it dilates the natural fracture, causing excessive leak-off. Potluri et al. (2005) analytically and numerically presented criteria to predict the manner in which a hydraulic fracture will propagate when it intersects a natural fracture. They

Manuscript received by the Editor 29 January 2011; revised manuscript received 8 June 2011; published online 30 December 2011.

¹University of Toronto, Toronto, Canada; presently at Applied Seismology Consultants, Shrewsbury, U.K. E-mail: xueping@appliedseismology.com.

²University of Toronto, Toronto, Canada. E-mail: paul.young@utoronto.ca.

© 2011 Society of Exploration Geophysicists. All rights reserved.

addressed the fact that there were three possible subsequent modes of fracture propagation, depending on the conditions of the horizontal stress contrast; the angle of intersection between the propagating fracture and the natural fracture, fracture toughness (a material property that describes the material resistance to fracture growth), and pressure drop within the natural fracture. Furthermore, Zhou et al. (2008) conducted a series of servo-controlled triaxial fracturing experiments on cement-sand blocks with three types of papers (rice paper, printer paper, and wrapping paper) acting as preexisting fractures with different frictional characteristics. They observed three interaction types (cross, dilate, and arrest) between induced fractures with preexisting fractures, depending on the differential horizontal stresses, the angle of approach, and the shear strength of the preexisting fracture. Observations similar to Blanton (1986) were made with respect to the influence of the differential stress conditions and angle of approach on whether the hydraulic fracture crossed or opened the preexisting fracture. Field work undertaken in naturally fractured formations reveal that the effects of natural fractures on fracture propagation are enhanced fluid leak-off, premature screen-out, arrest of the fracture propagation, formation of multiple fractures, fracture offsets, and high net pressures (Britt and Hager, 1994; Vinod et al., 1997; Rodgerson, 2000; Azeemuddin et al., 2002; Sharma et al., 2004).

Passive MS monitoring provides a unique tool to monitor the evolution of fluid injection around the treated rock reservoir, and seismic source mechanisms can yield information about the nature of deformation. However, field observations record only a portion of the activity, depending on the sensitivity of the monitoring system, and the high S/P-wave amplitude ratio (a common situation in hydraulic fracturing) limits the availability of recorded MS data when using traditional arrival-time-based location methods (Zhao et al., 2010). Furthermore, with use of predominantly single monitoring wells, the failure source mechanisms of microseismicity induced by hydraulic fracturing operations are unresolved, and we are unable to confirm induced tensile fractures suggested by theory (Economides and Nolte, 2000; Akulich and Zvyagin, 2008) and shear failure along pre-existing but isolated natural fractures (Rutledge and Phillips, 2003; Maxwell et al., 2010), although Šílený et al. (2009) concluded that double-couple shear failure need not be the dominant process in the microseismicity induced by hydrofracture treatments. In addition, there is a suggestion that hydrofracture growth may not be symmetric from the injection borehole (Fischer et al., 2008), which could be the result of the position of the monitoring system and its magnitude-distance detection threshold (Rutledge and Phillips, 2003) or caused by preexisting natural fractures (Sharma et al., 2004). For these reasons, numerical simulations could be a good choice to examine these effects, because in the model we could directly observe and analyze all activities within the configured boundary conditions, including MS and associated source mechanism, fluid network, and induced fractures. Some attempts have been made to use the discrete-element method (DEM) in which the rock mass is divided into deformable blocks or rigid particles with fluid flowing between them (Jing et al., 2001). Hazzard et al. (2002) developed a DEM to model the fluid injection in a hot dry rock reservoir. They produced realistic fluid pressure histories, realistic seismic source parameters, and asymmetrical growth

of hydrofractures, but they included a random network of joints instead of realistic joint geometries, and also did not consider the mechanical changes in domain volumes causing changes in domain pressures. Moreover, there are still issues that cannot be understood from the MS data alone, including the relationship between the fluid front and induced fracture, and the location and nature of any aseismic deformation.

A fully dynamic 2D distinct-element particle flow code model was tested with respect to simulating fluid injection into a reservoir containing a natural fracture, by comparing modeling geometries of hydraulic fractures and induced seismicity with actual results in laboratory experiments presented by Zhou et al. (2008) and fluid stimulation in a tight gas sand at Dowdy Ranch field, USA (Sharma et al., 2004). As would be expected, the 2D nature of the model limits direct comparisons with 3D field observations, such as fluid injection rate, seismic locations, or lateral and vertical hydrofracture growth. However, the model enables us to examine in detail the interaction between fluid pressure, rock deformation, and slip on existing fractures. The tested numerical models can help elucidate our understanding of the mechanics underlying seismicity, and can also provide insight on the relationship between seismicity, stress/damage, and the fluid front.

METHODOLOGY

Particle flow code (PFC)

The particle flow code in two dimensions (PFC^{2D}) is a distinct element geomechanical modeling program in which the rock material is modeled as an assembly of rigid round particles (unit-thickness disks). Contacts between the particles are assigned normal and shear stiffnesses, together with tensile and shear strengths, to model deformable and breakable bonds according to the relations described by Potyondy and Cundall (2004). Normally, the specified contact microstiffnesses influence the global macro stiffness (Young's modulus) of the rock being modeled. The ratio of normal-to-shear stiffness influences the Poisson's ratio of the rock. The measured macroscopic strength can be calibrated either to unconfined compressive strength or to Brazilian indirect tensile strength. The microstiffness and microstrength of particles can then be adjusted to reproduce realistic macrorock behavior. Under the applied load, if the maximum tensile or shear stress acting on a bond exceeds the tensile or shear strength of the bond, then the bond breaks, resulting in a tensile or shear crack, respectively. By further generation of these microcracks, a fracture can develop from the linking of individual microcracks. PFC has been applied to study mechanical behavior of sandstones, granites, and other rocks under different stress conditions with much success, including thermal fracturing experiments (Wanne and Young, 2008), hydraulic fracturing (Al-Busaidi et al., 2005), seismic velocities (Hazzard and Young, 2004b), in-situ failure tests (Potyondy and Autio, 2001), and large-scale underground excavations (Cai et al., 2007). A thorough description of the PFC model for rocks is given by Potyondy and Cundall (2004).

According to the studies by Potyondy and Cundall (2004), the particle size is an intrinsic part of the material characterization that affects the Brazilian indirect tensile strength (σ_t). Thus, particle size cannot be regarded as a free parameter that only controls model resolution; instead, it affects the fracture toughness. Potyondy

and Cundall (2004) noted that the fracture toughness (K_{lc}) scaling goes by the product of the tensile strength (σ_t) and the square root of the grain radius (r) for real rocks. Therefore, for a sample in the DEM, we have

$$K_{lc} \propto \sigma_t \sqrt{r}. \quad (1)$$

Synthetic seismicity in PFC

PFC uses an explicit approach to solve the equation of motion. This allows a dynamic simulation in which seismic waves propagate out from new faults and fractures. Each bond breakage is assumed to be a microcrack. The crack location is assumed to be the contact between the two particles, and the orientation of the crack is assumed to be perpendicular to the line joining the two centers. Microcracks occurring closely in both space and time are considered a single seismic event, if the models are run dynamically, by specifying low levels of numerical damping that simulates realistic levels of attenuation in the rock (Hazzard and Young, 2004a). Seismic source information can therefore be calculated for seismicity.

As described by Hazzard and Young (2002), when a bond breaks, the two particles on either side of the crack (the source particles) will move and contacts surrounding the source particles will experience some deformation. There will therefore be a force change at the surrounding contacts due to the formation of the crack. A summation is then performed around the contacts surrounding the crack to calculate components of the moment tensor from the contact locations and force changes. The moment tensor can be decomposed into isotropic and deviatoric components to help analyze the nature of the event as well as the moment magnitude (Feignier and Young, 1992). Furthermore, the moment tensor is calculated for each time step over the duration of the event. The duration of an event is determined by assuming that a shear fracture propagates at half the shear wave velocity of the rock (Madariaga, 1976) to the edge of the source area (one particle diameter). If another crack forms adjacent to the active crack such that the source areas overlap within the duration of the event, then the cracks are considered part of the same event. In this way, events made up of multiple cracks can exist, and more realistic magnitude distributions are achieved. The event centroid is assumed to be the location of the previously bonded contact. If more than one bond breakage makes up the event, then the geometrical center of the event is used. The occurrence time of the event is assumed to the time of maximum scalar moment (Hazzard and Young, 2002). An example of a synthetic seismic event is illustrated in Appendix A.

Fluid flow modeling in PFC

A technique for simulating fluid flow in PFC is adapted from the algorithm by Cundall (2000). Cundall's fluid flow is simulated by assuming that each particle contact is a flow channel (pipe) and that these channels connect small reservoirs that store some fluid pressure. As shown in Figure 1, the fluid network topology is generated by drawing lines between the centers of all particles in contact. This creates a series of enclosed domains. The center of each of these domains is stored as a reservoir. The reservoirs are then connected by pipes. Each particle contact corresponds to one pipe with a length related to two particle radii at the contact. Therefore,

each reservoir is surrounded completely by contacts and has some volume (void space in an enclosed domain) associated with it. A contact in which the particles are just touching is assumed to have residual aperture that allows fluid to flow. This is thought to be a realistic assumption since laboratory studies have shown that rock faces in contact always exhibit some residual aperture (Cook, 1992). When the contact is in compression, the aperture decreases as a function of the normal force at the contact. A thorough description of the mathematical equations for the fluid network in PFC was given by Al-Busaidi et al. (2005) and Zhao and Young (2009).

For a 2D fluid network model, fluid flow through a pipe is approximated by laminar flow through parallel plates with some aperture associated with it. The rate of volumetric flow (Q) is controlled by the Darcy's law (Bear, 1972). Fluid pressures stored in the domains are updated during the fluid calculation and act on the surrounding particles as equivalent body forces. Each domain receives flow from the surrounding pipes ($\sum Q$). In one time step (Δt), the fluid pressure change (ΔP) in each domain can then be calculated from the fluid bulk modulus (K_f) and the apparent volume change of the domain (ΔV), by applying the continuity equation (Itasca, 2005)

$$\Delta P = \frac{K_f}{V} \left(\sum Q \Delta t - \Delta V \right). \quad (2)$$

The second term in the equation represents the mechanical change in volume of the domain. Hazzard et al. (2002) and Al-Busaidi et al. (2005) considered the mechanical term negligible and did not include it in the calculation of domain pressure changes. However, this may not be the case in reality because the pressure variation caused by domain volumetric change could be significant especially for the areas with induced and natural fractures. Therefore, in this paper we use equation 2 in its entirety to enable the full hydro-mechanical coupling. Furthermore, to mimic a natural fracture in the model: Both normal and shear bonds are weakened compared with their intact strength along the line of the preexisting fracture, and residual apertures of the pipes along the line of the

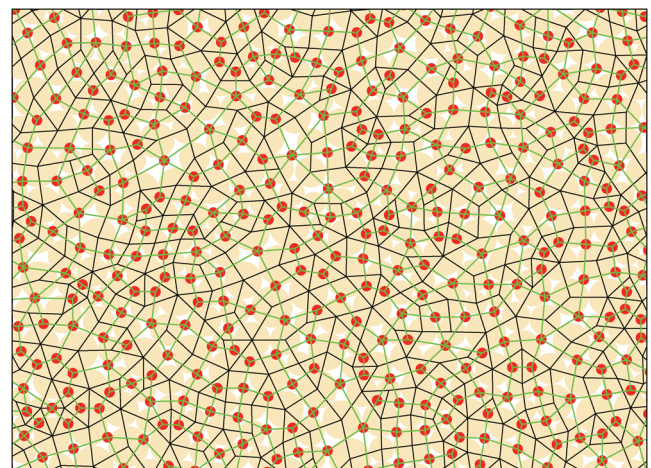


Figure 1. The fluid network modelled in PFC^{2D}, including solid particles (light orange circles), contacts (black lines), flow pipes (green lines), and fluid domains (solid red circles).

preexisting fracture are increased, resulting in an increased fracture permeability.

HYDRAULIC FRACTURE MODELING AT THE LABORATORY SCALE

Zhou et al. (2008) conducted a series of servo-controlled triaxial fracturing experiments to study the hydraulic fracture propagation behavior and fracture geometry in naturally fractured cubic cement-sand blocks of 300 mm. Figure 2 shows the schematic plan view of a hydraulic fracture intersecting a preexisting fracture for the laboratory experiments under a normal-faulting stress regime. The fluid pressure is applied in the center wellbore. Along the direction of hydraulic fracture propagation in the far field, parallel to the direction of maximum horizontal stress σ_2 (σ_3 is the minimum horizontal stress), the fracture intersects with a single closed natural fracture with an angle of approach θ . According to the Mohr-Coulomb criteria (Jaeger et al., 2007), slip occurs if the shear stress (τ), resulting from the normal stress (σ_n) and pore pressure acting on the plane of the natural fractures, is higher than the shear stress encountering the Mohr-Coulomb failure envelope.

Zhou et al. (2008) used three types of paper (rice paper, printer paper, and wrapping paper) with different thicknesses incorporated into cubic blocks to simulate natural fractures, and then tested under true triaxial loading. The friction coefficient and cohesion of the preexisting fracture were obtained from direct shear tests, which can be used to estimate the shear strength of the preexisting fracture, as well as to compare it to the unconfined compressive strength of the sample to find the strength ratio between the fracture and the intact rock. After simulating a hydraulic fracture, they observed three interaction types (cross, dilate,

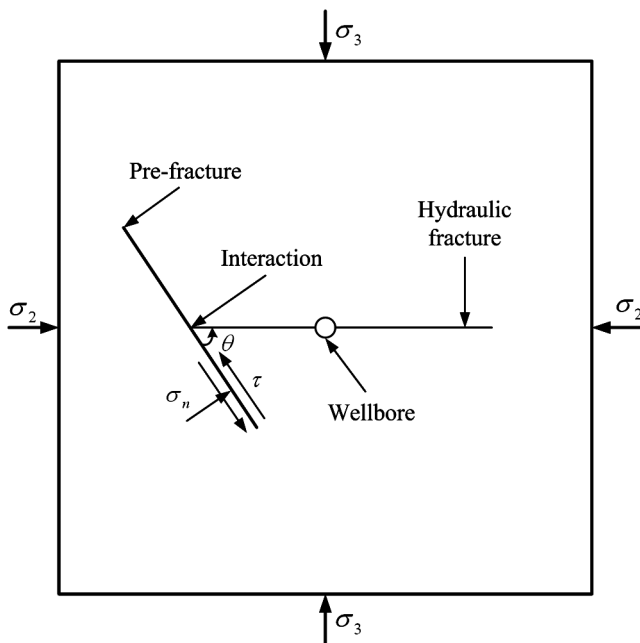


Figure 2. Schematic view of a hydraulic fracture intersecting a pre-existing fracture (after Zhou et al., 2008). σ_2 , σ_3 , θ , τ , and σ_n are the maximum horizontal stress, the minimum horizontal stress, the angle of approach, the shear stress, and the normal stress along the preexisting fracture.

and arrest) between the induced fracture and preexisting fracture depending on the horizontal differential stress ($\Delta\sigma = \sigma_2 - \sigma_3$), angle of approach (θ), and shear strength of the preexisting fracture.

In this paper, PFC is utilized to model the fluid stimulation based on the results from Zhou et al. (2008), specifically where printer paper was used to form the fracture. These are then examined in detail to provide insights into the mechanism underlying the induced fractures through the synthetic seismicity generated.

Model calibration

First, a set of biaxial and Brazilian tests was run to match the macroproperties of the laboratory rock, such as strengths and elastic properties, following the routine described by Potyondy and Cundall (2004). Table 1 lists the best fit parameters used for hydraulic fracturing models. For simplicity, the symbols in Table 1: r , L_d , L_h , L_t , E , ν , σ_c , σ_t , and q_i are the mean grain radius of sample, distance between the wellbore and the center of preexisting fracture, half-length of preexisting fracture, thickness of preexisting fracture, Young's modulus, Poisson's ratio, unconfined compressive strength, tensile strength, and fluid injection rate, respectively. To reduce the computation time, the sizes of particles in the model do not represent the actual grain sizes and in total there are 27,379 bonded particles composing the 300 × 300 mm sample. Accordingly, Figure 3 shows the naturally fractured laboratory reservoir model. Table 1 also provides the best fit model results, referring to the actual laboratory values, which indicates that the macroproperties (E , ν , and σ_c) are well reproduced by the PFC^{2D} model.

Note that the injection rate used in the model is much larger than the actual value, which is due to the fact that the current coarse model has a larger particle size than the actual grain size listed in Table 1. According to equation 1, the toughness of the current model is within an order of magnitude larger than that of the actual rock. As a result, the injection rate in the PFC model cannot be easily related to the actual injection rate because of higher fracture toughness and the 2D nature of the model, so a rate was chosen that was fast enough to induce fracturing and

Table 1. Best-fit parameters for lab hydraulic fracturing tests and PFC model calibration results.

Parameters	Laboratory ^a	Model
Sample	r (mm) E (GPa) ν σ_c (MPa) σ_t (MPa)	~0.09 8.402 0.23 28.34 b ~40 ~40 ~40 0.11 ~5
Prefracture	L_d (mm) L_h (mm) L_t (mm)	8.323 0.23 28.49 6.38 ~40 ~40 ~40 0.11 ~5
Fluid	q_i (m^3/s)	4.2×10^{-9} 1×10^{-6}

^aFrom Zhou et al. (2008).

^bValues are unknown.

result in reasonable model run times and comparable synthetic seismicity, but slow enough to maintain stability.

Model results and discussion

For a series of hydraulic fracturing experiments on blocks with the printer paper as the preexisting fracture, Zhou et al. (2008) tested three interaction angles ($\theta = 30^\circ, 60^\circ$, and 90°) and four combinations of confining stresses ($\sigma_2 - \sigma_3 = 13$ MPa – 3 MPa, 10 MPa – 3 MPa, 10 MPa – 5 MPa, and 8 MPa – 5 MPa, i.e., the horizontal differential stress $\Delta\sigma = 10$ MPa, 7 MPa, 5 MPa, and 3 MPa). They found that the hydraulic fracture could cross the preexisting fracture, or be arrested by either the opening and dilating or shear slippage of the preexisting fracture, in response to the fluid flow redirected along the preexisting fracture. As shown in Figure 4 from the laboratory results, hydraulic fractures crossed the preexisting fracture only at high horizontal differential stress and angles of approach of 60° or higher; hydraulic fractures did not cross the preexisting fracture at low horizontal differential stress or low angles of approach, primarily because the fluid pressure in the hydraulic fracture was sufficient to open and divert fluid along the preexisting fracture. Moreover, hydraulic fractures were arrested by the shear slip along the preexisting fracture only at high differential stresses and at angles of approach of 30° (Zhou et al., 2008). These results are consistent with Blanton's (1986) and Warpinski and Teufel's (1987) experimental results.

Based on the parameters shown in Table 1, PFC was used to numerically model the laboratory hydraulic fracturing tests. Figure 4 also summarizes the modeling results including the resultant cracks, induced seismicity, and calculated moment tensors shown in Figures 5, 6, 7, 8, 9, 10, 11, 12, and 13 after the fluid injection of around 3 s. In addition, four more models at different $\Delta\sigma$ and θ as well as the laboratory experiments by Zhou et al. (2008), were

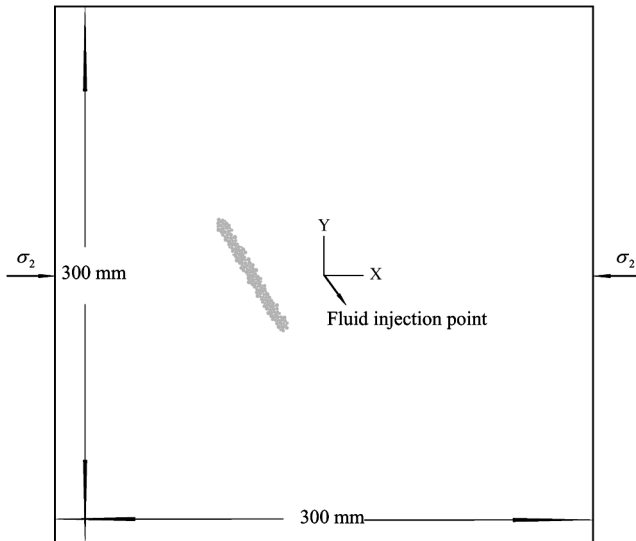


Figure 3. Naturally fractured laboratory reservoir model with $\theta = 60^\circ$ in PFC^{2D}. The center of the sample is selected as the fluid injection point. The particles within the preexisting fracture are colored in grey. The sample dimension is 300×300 mm and σ_2 is the maximum horizontal stress.

run to test the crossed and dilated trends shown in Figure 4. As shown in Figure 2, for each model the confining stresses were applied along the same directions. The height of each subfigure was less than 300 mm after being clipped, since the cut sections were not of interest here. The process and mechanics of hydraulic fracturing and the interaction between the preexisting and hydraulic fractures are discussed in detail below.

By virtue of the modeling, we can examine in detail the propagation of cracks outside and within the preexisting fracture and the evolution of induced seismicity and its mechanism. In Figure 5a, at $\Delta\sigma = 10$ MPa the induced fractures were clearly arrested by the preexisting fracture and higher fluid pressure was accumulated in front of the preexisting fracture. A large number of shear cracks were produced along the preexisting fracture. Compared to induced seismicity in Figure 8a and the moment tensors in Figure 11a, Figure 14 shows only shear events and corresponding moment tensors after the fluid injection of about 4 s. At the interaction region between preexisting and hydraulic fractures (Fig. 14), shear events were triggered and propagated along the preexisting fracture, but seldom ran through the fracture, which confirms that the fracture arrest was caused by the shear slip of the preexisting fracture. This was also the mechanical reason for the much lower fluid pressure within the preexisting fracture. Interestingly, Figure 14 also illustrates that shear events accompanied the propagation of hydraulic fractures. The fracture tip tends to be ahead of the fluid front in the current case. In general, as shown in Figures 5, 6, and 7, the higher the $\Delta\sigma$, the higher the likelihood of the fracture tip moving ahead of the fluid front.

Sometimes the fracture arrest and dilation are not easy to distinguish, since both could arrest the hydraulic fractures, at least temporally. Nevertheless, the dilation usually results in fluid flow

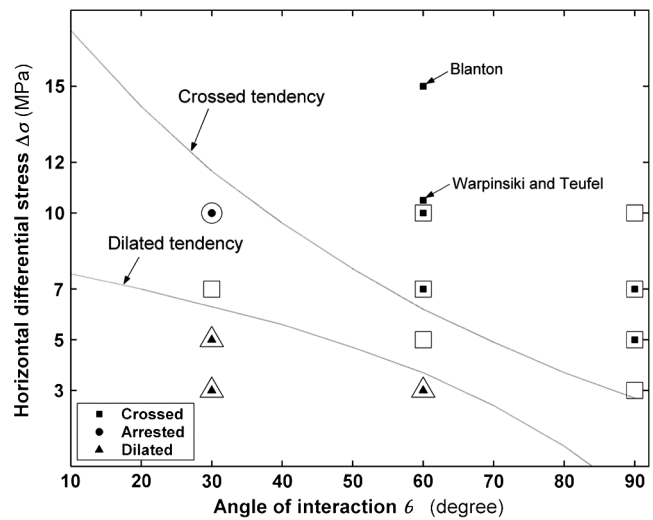


Figure 4. Laboratory (smaller solid symbols) (Zhou et al., 2008) and model (larger symbols) results showing the hydraulic fracture behavior for the printer paper as the preexisting fracture. $\Delta\sigma$ and θ are the horizontal differential stress and the angle of approach. The crossed and dilated tendency lines were from Zhou et al. (2008) who estimated these based on their laboratory testing results. Four additional models, i.e., $\Delta\sigma = 10$ MPa at $\theta = 90^\circ$, $\Delta\sigma = 7$ MPa at $\theta = 30^\circ$, $\Delta\sigma = 5$ MPa at $\theta = 60^\circ$, and $\Delta\sigma = 3$ MPa at $\theta = 90^\circ$, were run to test the crossed and dilated tendency lines.

along the preexisting fracture or a high-pressure accumulation around preexisting fracture. The evolution of seismicity, as shown in Figures 8, 9, and 10, was used to ascertain whether the hydraulic fractures were arrested temporally. As shown in Figures 5c, 5d, 8c, and 8d, the interaction types for $\Delta\sigma = 5 \text{ MPa}$ and 3 MPa at $\theta = 30^\circ$ are thus regarded as the fracture dilation, since the induced seismicity propagated along the preexisting fracture for a certain period of time after the hydraulic fractures interacted with the preexisting fracture. More importantly, there was a significant amount of accumulated fluid pressure around the preexisting fracture, compared to the situation of $\Delta\sigma = 10 \text{ MPa}$ at $\theta = 30^\circ$.

Figure 5. Induced cracks (marked by black/red lines corresponding to tensile/shear cracks) and fluid flow (marked by light blue circles whose sizes are scaled to 40 MPa) under different $\Delta\sigma$ at $\theta = 30^\circ$ after an injection of about 3 s. The width of each subfigure is 300 mm. The injection point is located at the center of each subfigure that is the same as Figure 2. The light gray solid circles are particles within the preexisting fracture.

In the case of dilation, for $\Delta\sigma = 5 \text{ MPa}$ at $\theta = 30^\circ$, the preexisting fracture was opened by the large tensile force at the interaction between the preexisting fracture and induced fracture shown in Figures 8c and 11c. The high fluid pressure in Figure 5c and 5d dominated a much larger region than the case of the fracture arrest in Figure 5a, which may result from the increasing leak-off into the preexisting fracture as mentioned by Warpinski (1991). Moreover, the hydraulic fracture was arrested temporarily by opening and dilating the preexisting fracture, which agrees with the interaction criterion described by Potluri et al. (2005). Similar to the case of $\Delta\sigma = 3 \text{ MPa}$ at $\theta = 60^\circ$ in Figures 6d

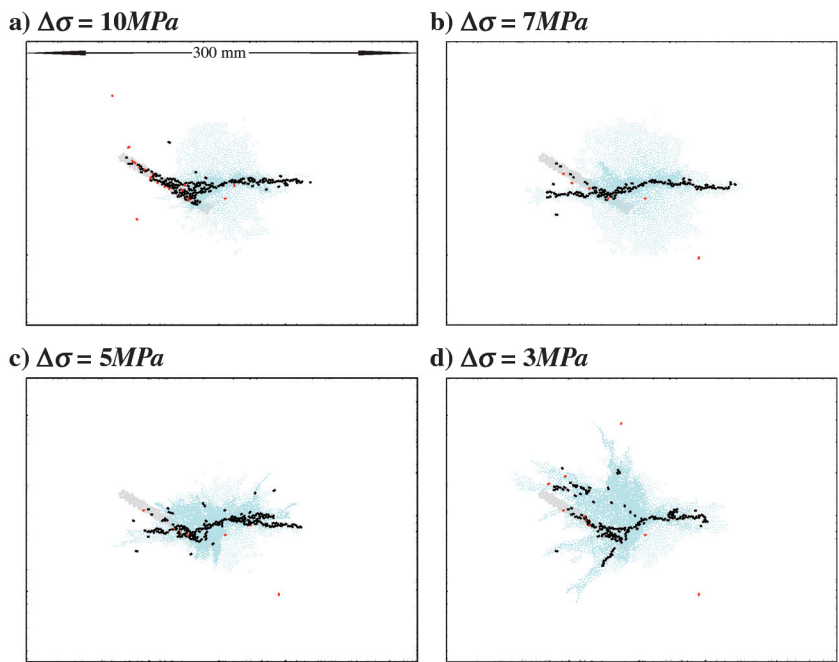
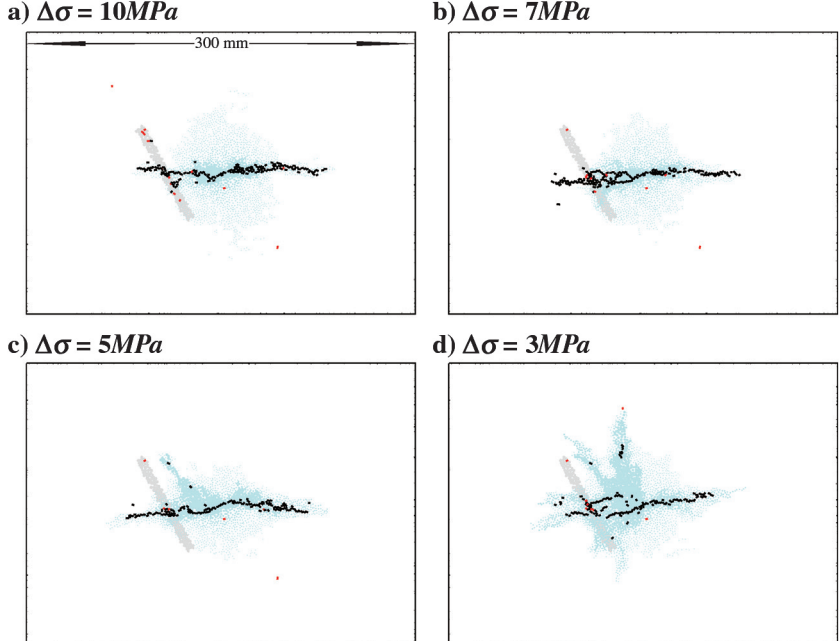


Figure 6. Induced cracks and fluid flow under different $\Delta\sigma$ at $\theta = 60^\circ$ after an injection of about 3 s. The marks have the same meanings as Figure 5.



and 9d, the hydraulic fracture was arrested temporarily by opening and dilating the preexisting fracture, which agrees with the interaction criterion described by Potluri et al. (2005). On the other hand, for $\Delta\sigma = 3 \text{ MPa}$ at $\theta = 30^\circ$ in Figures 5d and 8d, the hydraulic fractures were almost arrested along the direction of the maximum horizontal stress by opening and dilating the preexisting fracture with a significant resultant fluid flow around the preexisting fracture. In this case, a branch of hydraulic fractures finally detoured nearly 90° away from the lower end of the preexisting

fracture. As shown in Figure 8d, the occurrence times of the corresponding seismicity were directly affected by the distance between the injection center and the lower edge of the preexisting fracture. As a result, the fluid pressure, as well as fractures and seismicity, was accumulated earlier close to the lower boundary of the preexisting fracture.

In the case of crossing, the preexisting fracture can be easily bisected by a single hydraulic fracture when $\Delta\sigma = 10 \text{ MPa}$ and 7MPa at $\theta = 90^\circ$, as shown in Figure 7a and 7b. Hydraulic

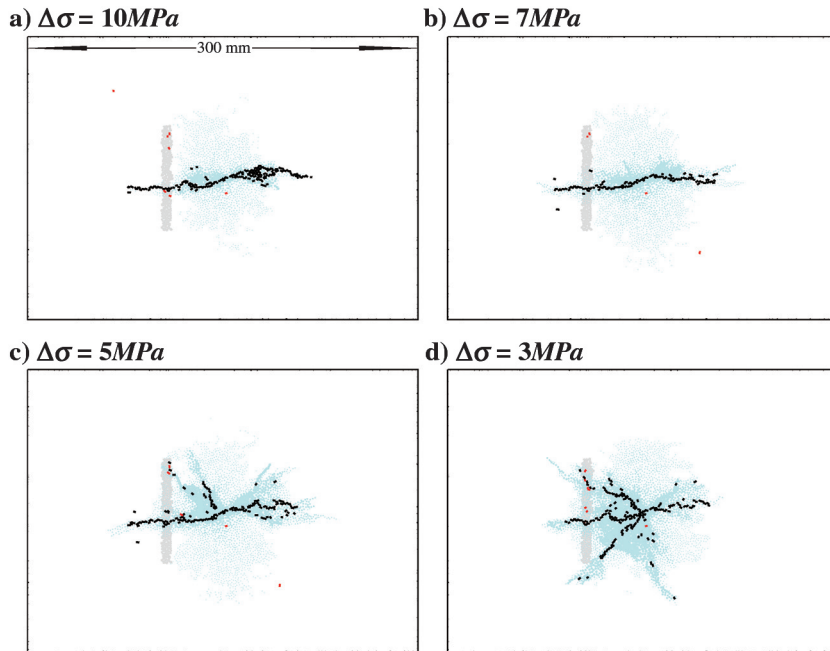


Figure 7. Induced cracks and fluid flow under different $\Delta\sigma$ at $\theta = 90^\circ$ after an injection of about 3 s. The marks have the same meanings as Figure 5.

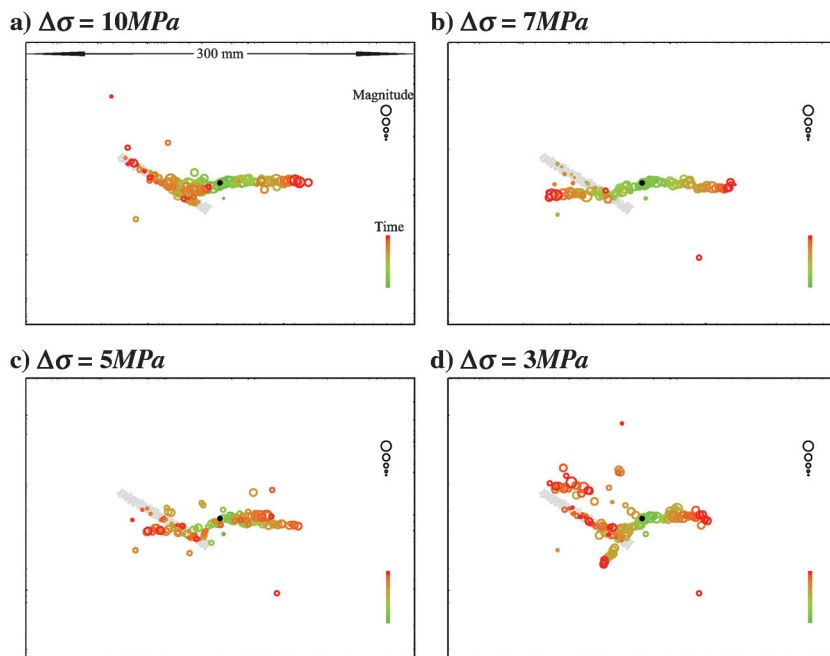


Figure 8. Induced seismicity for different $\Delta\sigma$ at $\theta = 30^\circ$ after an injection of about 3 s. The width of each subfigure is 300 mm. The sizes of seismic events are scaled according to their magnitudes and the color corresponds to the occurring time of seismic events (green/red = early/late). The central injection point is indicated by the black filled circle.

fractures can break out of the preexisting fracture with some offsets when $\Delta\sigma = 10$ MPa, 7 MPa, and 5 MPa at $\theta = 60^\circ$, as well as $\Delta\sigma = 7$ MPa at $\theta = 30^\circ$, as shown in Figure 6a and 6c and Figure 5b. Moreover, multiple fractures can be induced and fractures seem to propagate through the tip of the preexisting fracture when $\Delta\sigma = 5$ MPa and 3 MPa at $\theta = 90^\circ$, as shown in Figure 7c and 7d. These three modeled crossing types are also consistent with the three possible modes of fracture growth described by Potluri et al. (2005). In addition, the higher the $\Delta\sigma$, the fewer the multiple branches for induced fractures.

Figure 9. Induced seismicity for different $\Delta\sigma$ at $\theta = 60^\circ$ after an injection of about 3 s. The marks have the same meanings as Figure 8.

As shown in Figures 8, 9, and 10, a significant number of seismic events form away from the high-pressure areas in each case, especially with lower $\Delta\sigma$. As indicated by the times at which seismic events occurred, it appears that hydraulic fractures simultaneously propagate in opposite directions, away from the central injection area. After induced fractures reach the preexisting fracture, it seems that the interaction between the natural and induced fractures dominates the process. There is more seismicity triggered close to the preexisting fracture, due to the accumulation of higher fluid pressures. Note that the asymmetrical distribution of seismicity may result from the preexisting

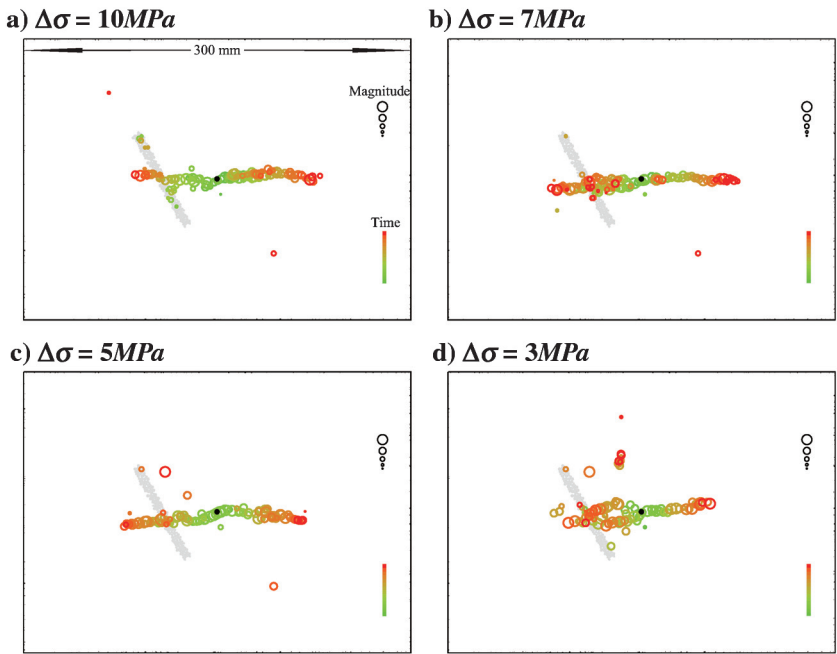
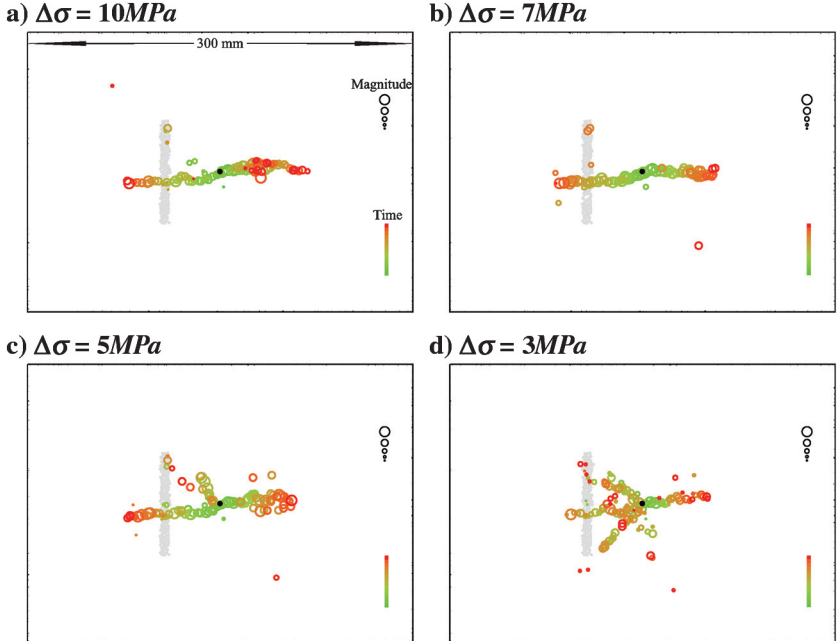


Figure 10. Induced seismicity for different $\Delta\sigma$ at $\theta = 90^\circ$ after an injection of about 3 s. The marks have the same meanings as Figure 8.



fracture. Furthermore, the moment tensors shown in all cases reveal that the hydraulic fractures are opened subparallel to the minimum horizontal principal stress outside the preexisting fracture and subperpendicular to the preexisting fracture within the preexisting fracture. At the same time, the forces capable of crossing the preexisting fracture are generally much smaller than those cracking particles outside the preexisting fracture, except for the fracture arrest case. As a whole, the interactions between the preexisting and hydraulic fractures are well captured by the PFC models, and the model results provide detailed insights into the mechanism. Additionally, the modeling results suggest that

the dilated and crossed tendency lines described by Zhou et al. (2008) need to be adjusted and the region of arrested behavior possibly decreased.

HYDRAULIC FRACTURE MODELING AT THE FIELD SCALE

As shown in the laboratory and corresponding modeling results, natural fractures can have a significant impact on fracture growth. This influence is more complex in the field because natural fractures vary across scales from a joint network to fault networks, although

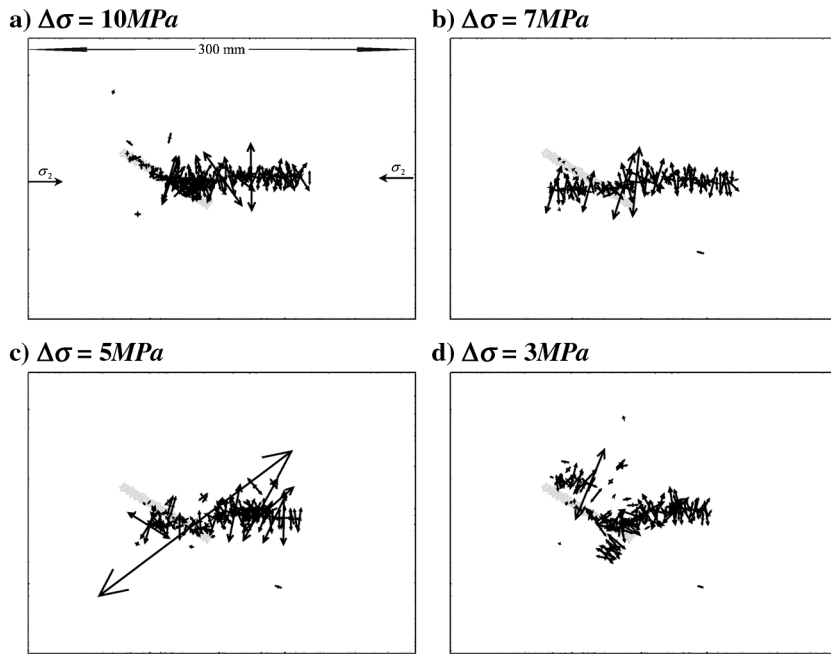


Figure 11. Moment tensors of induced seismicity corresponding to Figure 8 under different $\Delta\sigma$ at $\theta = 30^\circ$. σ_2 is the maximum horizontal stress. The light gray solid circles are particles within the preexisting fracture, and the width of each sub-figure is 300 mm. Note that moment tensors are plotted as equivalent forces, so that two sets of arrows of equal length but opposite polarity represent a perfect double-couple (shear) source.

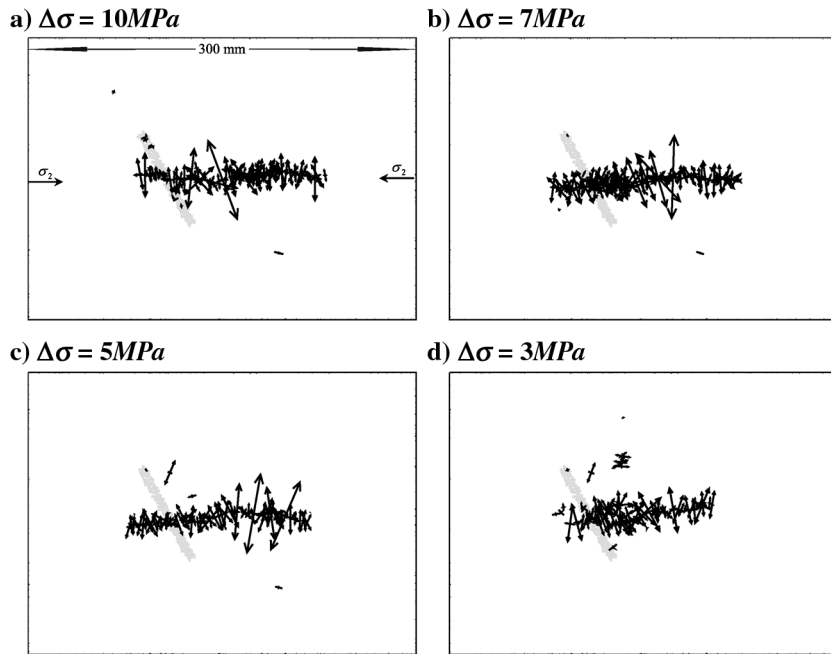


Figure 12. Moment tensors of induced seismicity corresponding to Figure 9 under different $\Delta\sigma$ at $\theta = 60^\circ$. The marks have the same meanings as Figure 11.

they are isolated or discrete. The analysis at the field scale presented here is based on the data sets of the Bonner layer stimulation in the Dowdy Ranch field, East Texas (Sharma et al., 2004). As shown in Figure 15, owing to the preexisting fault, the fracture growth was asymmetrical and arrested in the Bonner layer, but the Bonner treatment was observed to have communicated upward into the Moore and Bossier Marker sands through a fault (Sharma et al., 2004), resulting in a significant amount of out-of-zone fracture height growth as indicated by the migration of seismicity in space and time. Furthermore, propped or effective fracture half-length, derived from pressure build-up analysis and history matching, were significantly shorter than the created fracture half-length deduced from MS locations (Sharma et al., 2004). Since seismic events were recorded only by a single array of receivers in the field, it is difficult to solve for the seismic source mechanism (Fischer et al., 2008). Fortunately, we can examine the mechanics and mechanism by the direct observation of the numerical model.

Model calibration

Following a similar procedure to the previous laboratory hydraulic fracturing model, the calibrated bonded particle model was

created to simulate a 2D slice of the Bonner reservoir approximately 3974 m below the surface (the starting position for the fluid treatment). The 500×500 m model was made up of 13,880 particles with an average radius of 2 m to optimize calculation time. Clearly each particle does not represent a single mineral grain in the rock, and the particles are simply a way to discretize the medium. A physical interpretation of the particles might be blocks of sandstone separated by cohesive joints or planes of weakness.

The best-fit parameters and calibration results are shown in Table 2. Note that effective stress is assumed so that the applied stresses (σ_2 and σ_3) equal the actual in situ stresses, minus the pore fluid pressure. The tensile strength was calculated by use of the method described by Eaton (1975) when we estimated in-situ stresses and pore pressures assuming the overburden pressure gradient 22.6 KPa/m (1 psi/ft). In addition, estimated from the microseismic mapping result shown in Figure 15, the preexisting fault was created assuming $\theta = 120^\circ$, $L_d = \sim 50$ m, $L_h = \sim 43$ m, and $L_t = \sim 5.7$ m. According to equation 1 the toughness of the sample is about one order of magnitude larger than that of the real rocks for the current coarse model. The resultant higher injection rate in the model is attributed to the same factors as in the laboratory models mentioned in the laboratory model.

Figure 13. Moment tensors of induced seismicity corresponding to Figure 10 under different $\Delta\sigma$ at $\theta = 90^\circ$. The marks have the same meanings as Figure 11.

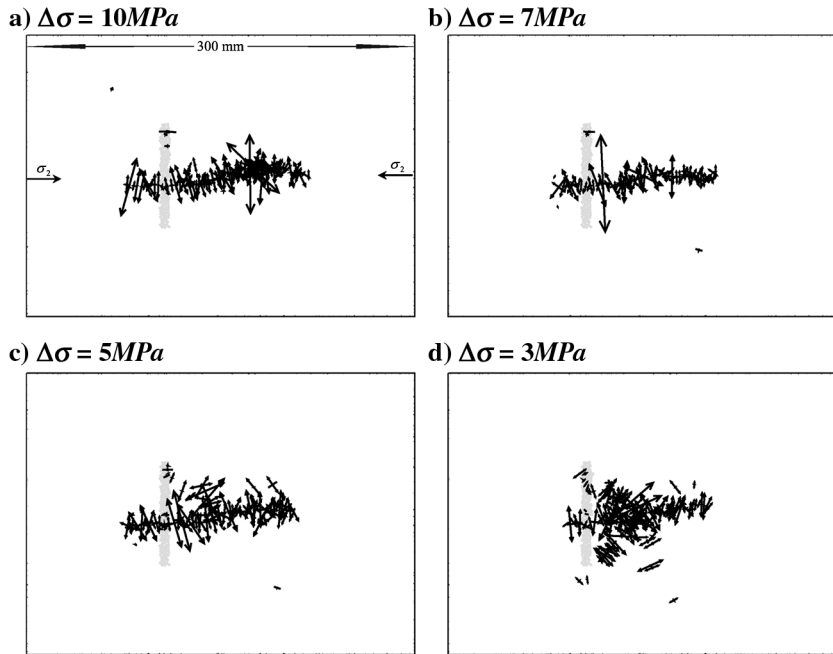
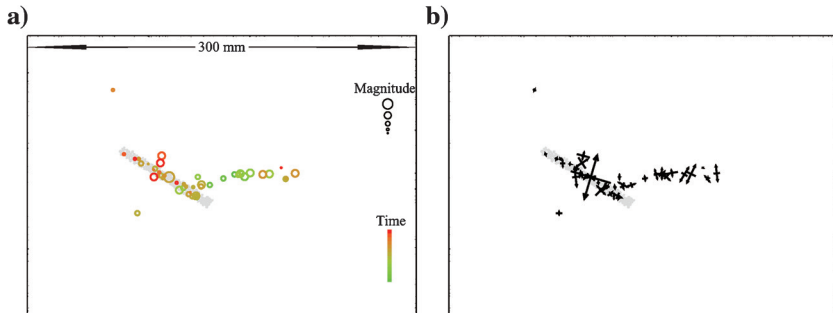


Figure 14. Induced shear events and corresponding moment tensors for $\Delta\sigma = 10$ MPa at $\theta = 30^\circ$ after an injection of about 4 s. The width of the subfigure is 300 mm. (a) Seismicity. The sizes of seismic events are scaled according to their magnitudes and the color corresponds to the occurring time of seismic events (green/red = early/late). (b) Moment tensors corresponding to (a).



Model results and discussion

Due to limitations in the microseismic monitoring configuration used in the field, which was restricted to the deployment of a string of geophones in a single borehole, the resulting data could not fully resolve source location and source mechanism information. However, through direct examination of the calibrated PFC model, the mechanics underlying the recorded MS events can be projected. Figure 16 shows the total induced MS events and associated moment tensors, cracks, and fluid flow after about a 3-hour fluid injection in the model. Compared to Figure 15b, Figure 16 illustrates that the PFC model produces a scope and orientation of induced MS events similar to results obtained from the actual recorded MS events, and that the range of moment magnitudes in the model (-1.51 – 0.61) is within an order of magnitude of the actual events recorded at Bonner (-0.93 – 1.15 , Pettitt and Young, 2007). This gives some confidence that the model is behaving in a realistic manner in consideration of the 2D nature of the current model.

Table 3 summarizes the results of the hydraulic fracturing of the naturally fractured field reservoir after about a 3-hour fluid injection. The tensile events dominated the propagation of hydraulic fracturing and the shear events only account for about 25% of the total induced MS. However, there are generally not enough events in the test to consider the statistics of the magnitude distributions. The reasons for the low number of MS events are twofold: First, the current model has a very low resolution; second, for the current synthetic seismic algorithm, once a bond along the preexisting fracture is broken, no more cracking or seismicity will be recorded, although unstable slip can occur and energy can be released (Marone, 1998), which could also result in a lower magnitude in the model as shown in the result above, and this must be accounted for in future developments.

A certain number of MS events seem to propagate out of the trajectory through the upper side of the fault, due to the opening of the fault. As a result, the hydraulic fracture was arrested initially, but extended further from the tip of the preexisting

fracture. The synthetic moment tensor result is used to illustrate the mechanics underlying the recorded MS event. As shown in Figure 17, the significant tensile event in Figure 16c actually includes a large amount of tensile and shear cracks within and outside the fault, which results in the opening and dilation of the preexisting fault. From this dilation and the fluid leakage as shown in Figure 16, we could expect the upper and lower layers were communicated through the preexisting fault, resulting in out-of-zone seismicity in the field. Furthermore, the induced cracks appeared to be ahead of the fluid front, indicating that there is a fluid lag between the fracture tip and the fluid front. Since a tip screenout did not occur during the hydraulic fracturing of Bonner sand (Sharma et al., 2004), the fluid lag together with the fluid leak-off imply that the effective or propped half-length is shorter than the generated fracture half-length deduced from MS locations. This agrees with the results derived from pressure buildup and history matching production data during the multistage fracturing treatment in the Bossier formation (Sharma et al., 2004). In addition, the interaction type between

Table 2. Best-fit parameters for Bonner stimulation and PFC model calibration results.

Parameters	Actual	Model
Sample	r (m)	$\sim 9 \times 10^{-5}$
	E (GPa)	44
	ν	0.22
	σ_c (MPa)	^a
	σ_t (MPa)	3.24
Reservoir	σ_1 (MPa)	6.3
	σ_3 (MPa) (mm)	9.6
Fluid	q_i (m^3/s)	8.7×10^{-6}
		1×10^{-3}

^aValues are unknown.

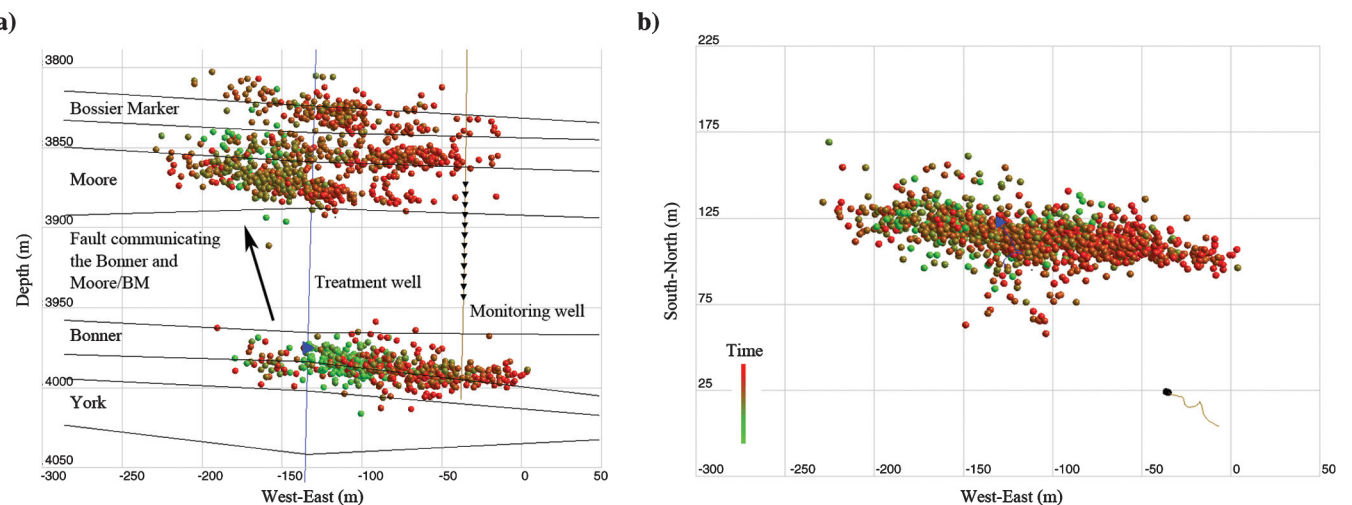


Figure 15. MS data (color-filled circles) recorded through the Bonner treatment. The color corresponds to the occurring time of MS events (green/red = early/late). A perforation shot (blue triangle) is located at the treatment well (blue line) within the Bonner layer and a linear receiver array (black triangles) is located at the monitoring well (brown line). (a) Side view; (b) plan view.

hydraulic and natural fractures is also located below the possible dilated tendency for the current $\Delta\sigma = 3.3$ MPa, as shown in Figure 4. Therefore, these matches strongly suggest that the model is behaving in a realistic way, and that levels of deformation and associated energy release are similar in the model and in the field. Because of the 2D nature of the model, it can only qualitatively capture the propagation of the out-of-zone seismicity recorded in the field. If a 3D model were run, a direct measurement of fracture volume and fluid leak-off calculation could be realized.

Table 3. Hydraulic fracturing modeling results for the Bonner treatment.

Parameters	Value
Number of cracks (normal/shear)	263 (228/35)
Number of induced MS events	52
Number of shear MS events	14
Number of explosive/implosive MS events	31/7
Magnitude of MS (Min/Max)	-1.52/0.61

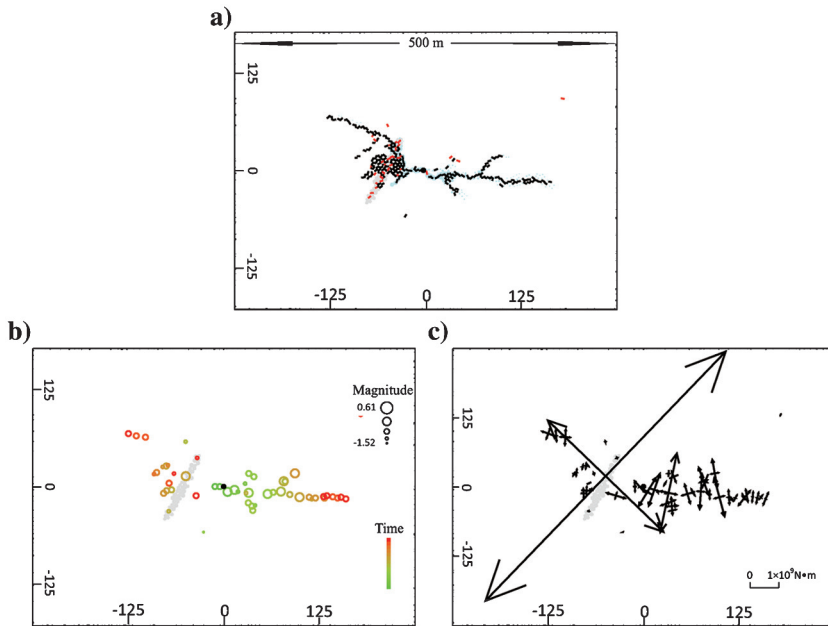


Figure 16. Induced cracks, fluid flow, MS, and moment tensors after an injection of about 3 hours in the field model. The fluid injection point is indicated by the black filled circle at the center of each subfigure, the width of each subfigure is 500 m, and the axis values are in meters. (a) Induced cracks (marked by black/red lines corresponding to tensile/shear cracks) and fluid flow (marked by light blue circles whose sizes are scaled to 40 MPa). (b) Synthetic MS events. The sizes of seismic events are scaled to the maximum magnitude of 0.61 and the color corresponds to the occurring time of seismic events (green/red = early/late). (c) Moment tensors corresponding to (b). The seismic moment is scaled to the maximum of 8.2×10^9 N · m.

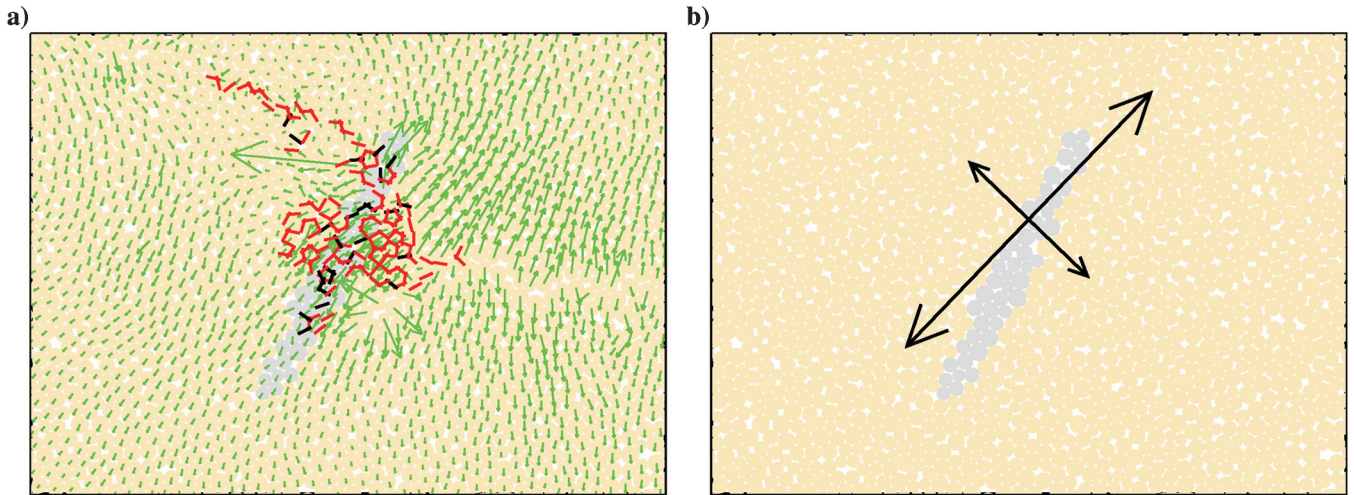


Figure 17. The tensile seismic event composed of 147 cracks corresponding to the largest event shown in Figure 16c. (a) Particle velocities (green arrows) after bond breakages. The crack is represented by a subvertical line (black for tensile and red for shear) between the two source particles. (b) The calculated moment tensor.

CONCLUSIONS

We have successfully tested a 2D discrete-element particle flow code model with fully dynamic and hydro-mechanical coupling, to simulate fluid stimulation on a reservoir containing a natural fracture by directly comparing the modeling geometries of hydraulic fractures and induced seismicity with actual laboratory and field data results. The numerical results qualitatively agree with the laboratory and field observations and confirm the possible mechanics of new fracture development and their interaction with natural fractures.

On the laboratory scale, the model captured three interaction types between preexisting and induced fractures. Depending on the differential stresses and orientations of the preexisting fracture, the model also verified three possible crossing modes of fracture growth. Through seismic mechanism analysis, the models confirmed that fracture arrest can be caused by the shear slippage of the preexisting fracture and that shear slippage can explain lower fluid pressures within the preexisting fracture. At the same time, the hydraulic fracture can also be arrested temporarily by opening and dilating the preexisting fracture, which may result in increased leak-off into the preexisting fracture. Furthermore, the less the differential stress, the more the fracture segments and the less the likelihood that the fracture tip will go ahead of the fluid front.

On the field scale, the model produced an extent and orientation of induced fractures similar to the results obtained in the actual recorded microseismicity. Moreover, the model showed the resultant fluid lag between the fracture tip and the fluid front and provided strong support for the hypothesis that the hydraulic fractures were arrested by the dilation of the fault. At the same time, the leakage of a large volume of fluid through the fault area was qualitatively predicted by the 2D model. This model observation was congruent with the engineering assessment that the propped half-length is shorter than the created fracture half-length as deduced from MS locations. The model is consistent with field observations and can assist in the interpretation both of the micromechanism underlying the induced fracture and of the relationship between the induced seismicity and the fluid front through direct observation of the model.

Admittedly, the model is still a gross simplification of the actual rock mass conditions. The low resolution, the 2D nature of the models, and the shortage of actual parameters, all particularly limit the possible quantitative comparisons with actual data. However, through the use of synthetic seismicity, moment tensors, and fractures, the current model clearly demonstrates not only the reasonable physical mechanics underlying the interaction between hydraulic and natural fractures, but also the relationship between the fluid front and the fracture tip, all of which are difficult to ascertain from field data. If a higher resolution was used with further development in the seismic monitoring algorithm to account for unstable slip along the preexisting fracture, then the model would produce a realistic injection rate and more synthetic seismicity for better comparisons with field data. Moreover, modeling results in 2D may not be fully representative of fluid properties (fluid volume and injection fluid rate) and, thus, of the total number of induced microcracks. Three-dimensional modeling is more realistic, allowing the use of a realistic fluid injection rate and examination of both lateral and vertical hydrofracture growth, especially for reservoirs with natural fractures, such as the Bonner treatment.

ACKNOWLEDGMENTS

The authors would like to acknowledge Applied Seismology Consultants and the Halliburton company for providing the hydraulic fracturing data sets. The authors would also like to thank Dr. Jim Hazzard for providing the basic PFC^{2D} fluid functions. A further acknowledgement goes to the four reviewers, and to the volume editor, whose comments have greatly improved this paper.

APPENDIX A

AN EXAMPLE OF A SYNTHETIC SEISMIC EVENT

According to the definitions by Feignier and Young (1992), an event will be considered predominantly implosive if the isotropic component is negative and makes up greater than 30% of the moment tensor. Similarly, an explosive event will be greater than 30% isotropic (positive). All other events are considered predominantly deviatoric (shear), i.e., its isotropic component is less than 30% of the moment tensor.

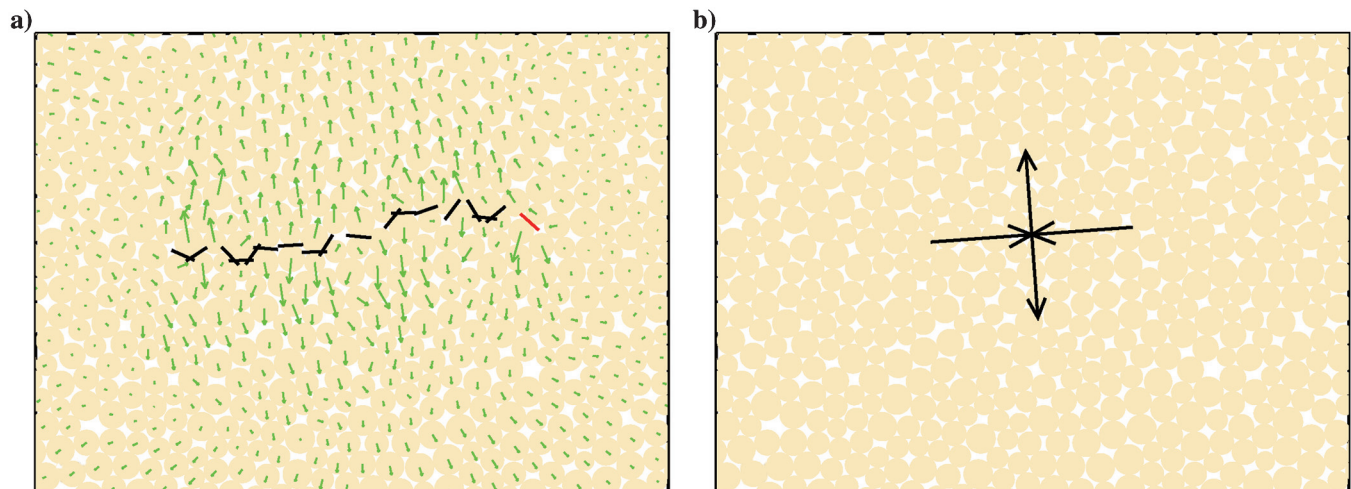


Figure A-1. An example synthetic seismic shear event composed of seventeen tensile cracks and one shear crack. (a) Particle velocities (green arrows) and cracks (black line for tensile crack and red line for shear crack); (b) the calculated moment tensor.

Figure A-1 shows an example of a synthetic seismic shear event resulting from a shear and several tension bond-breakages. The calculated moment tensor is shown in Figure A-1b. The moment tensor is plotted as equivalent forces (i.e., two arrows pointing away from each other indicate a tensile event, while two sets of arrows of equal length pointing in opposite directions indicate a double-couple, the signature of a shear event). The representation of the moment tensor demonstrates the principal values (eigenvalues) of the moment tensor matrix as sets of arrows whose direction and length indicate the orientation and magnitude, respectively, of the principal values. In addition, the PFC particle velocities show rapid shear motion.

REFERENCES

- Akulich, A. V., and A. V. Zvyagin, 2008, Interaction between hydraulic and natural fractures: *Fluid Dynamics*, **43**, no. 3, 428–435, doi: [10.1134/S0015462808030101](https://doi.org/10.1134/S0015462808030101).
- Al-Busaidi, A., J. F. Hazzard, and R. P. Young, 2005, Distinct element modeling of hydraulically fractured Lac du Bonnet granite: *Journal of Geophysical Research*, **110**, B06302, doi: [10.1029/2004JB003297](https://doi.org/10.1029/2004JB003297).
- Azeemuddin, M., S. G. Ghori, S. Saner, and M. N. Khan, 2002, Injection-induced hydraulic fracturing in a naturally fractured carbonate reservoir: A case study from Saudi Arabia: Presented at the International Symposium & Exhibition on Formation Damage Control, SPE.
- Bear, J., 1972, *Dynamics of fluids in porous media*: American Elsevier Publishing Company, Inc.
- Blanton, T. L., 1986, Propagation of hydraulically and dynamically induced fractures in naturally fractured reservoirs: Presented at the unconventional gas technology symposium, SPE/DOE.
- Britt, L. K., and C. J. Hager, 1994, Hydraulic fracturing in a naturally fractured reservoir: Presented at the International Petroleum Conference and Exhibition, SPE.
- Cai, M., P. K. Kaiser, H. Morioka, M. Minami, T. Maejima, Y. Tasaka, and H. Kurose, 2007, FLAC/PFC coupled numerical simulation of AE in large-scale underground excavations: *International Journal of Rock Mechanics and Mining Sciences & Geomechanics Abstracts*, **44**, no. 4, 550–564, doi: [10.1016/j.ijrmms.2006.09.013](https://doi.org/10.1016/j.ijrmms.2006.09.013).
- Cook, N. G. W., 1992, Natural joints in rock: Mechanical, hydraulic and seismic behaviour and properties under normal stress: *International Journal of Rock Mechanics and Mining Sciences & Geomechanics Abstracts*, **29**, no. 3, 198–223, doi: [10.1016/0148-9062\(92\)93656-5](https://doi.org/10.1016/0148-9062(92)93656-5).
- Cundall, P., 2000, Fluid formulation for PFC^{2D}: Itasca Consulting Group.
- Eaton, B. A., 1975, The equation for geopressure prediction from well logs: Presented at the Fall Meeting of the SPE of AIME, SPE.
- Economides, M. J., and K. G. Nolte, 2000, *Reservoir stimulation* (3rd edition): Prentice Hall.
- Feignier, B., and R. P. Young, 1992, Moment tensor inversion of induced microseismic events—evidence of nonshear failures in the $-4 < M < -2$ moment magnitude range: *Geophysical Research Letters*, **19**, 1503–1506, doi: [10.1029/92GL01130](https://doi.org/10.1029/92GL01130).
- Fischer, T., S. Hainzl, L. Eisner, S. A. Shapiro, and J. Le Calvez, 2008, Microseismic signatures of hydraulic fracture growth in sediment formations: Observations and modeling: *Journal of Geophysical Research*, **113**, B02307, doi: [10.1029/2007JB005070](https://doi.org/10.1029/2007JB005070).
- Hazzard, J. F., and R. P. Young, 2002, Moment tensors and micromechanical models: *Tectonophysics*, **356**, 181–197, doi: [10.1016/S0040-1951\(02\)00384-0](https://doi.org/10.1016/S0040-1951(02)00384-0).
- Hazzard, J. F., and R. P. Young, 2004b, Numerical investigation of induced cracking and seismic velocity changes in brittle rock: *Geophysical Research Letters*, **31**, L01604, doi: [10.1029/2003GL019190](https://doi.org/10.1029/2003GL019190).
- Hazzard, J. F., and R. P. Young, 2004a, Dynamic modelling of induced seismicity: *International Journal of Rock Mechanics and Mining Sciences & Geomechanics Abstracts*, **41**, no. 8, 1365–1376, doi: [10.1016/j.ijrmms.2004.09.005](https://doi.org/10.1016/j.ijrmms.2004.09.005).
- Hazzard, J. F., R. P. Young, and S. J. Oates, 2002, Numerical modelling of seismicity induced by fluid injection in a fractured reservoir: Proceedings of 5th North American Rock Mechanics Symposium, NARMS-TAC, 1023–1030.
- ITASCA CONSULTING GROUP INC., 2005, PFC^{3D}, Verification problems & example applications volume, version 3.1: Itasca.
- Jaeger, J. C., N. G. W. Cook, and R. W. Zimmerman, 2007, *Fundamentals of rock mechanics*: Blackwell.
- Jing, L., Y. Ma, and Z. Fang, 2001, Modeling of fluid flow and solid deformation for fractured rocks with discontinuous deformation analysis (DDA) method: *International Journal of Rock Mechanics and Mining Sciences*, **38**, no. 3, 343–355, doi: [10.1016/S1365-1609\(01\)00005-3](https://doi.org/10.1016/S1365-1609(01)00005-3).
- Lumley, D., D. Adams, R. Wright, D. Markus, and S. Cole, 2008, Seismic monitoring of CO₂ geo-sequestration: Realistic capabilities and limitations: 78th Annual International Meeting, SEG, Expanded Abstracts, 2841–2845.
- Madariaga, R., 1976, Dynamics of an expanding circular fault: *Bulletin of the Seismological Society of America*, **66**, 639–666.
- Marone, C., 1998, Laboratory-derived friction laws and their application to seismic faulting: *Annual Review of Earth and Planetary Sciences*, **26**, 643–696, doi: [10.1146/annurev.earth.26.1.643](https://doi.org/10.1146/annurev.earth.26.1.643).
- Maxwell, S. C., J. Rutledge, R. Jones, and M. Fehler, 2010, Petroleum reservoir characterization using downhole microseismic monitoring: *Geophysics*, **75**, no. 5, A129–A137, doi: [10.1190/1.347796](https://doi.org/10.1190/1.347796).
- Maxwell, S. C., and T. Urbancic, 2001, The role of passive microseismic monitoring in the instrumented oil field: *The Leading Edge*, **20**, 636–639, doi: [10.1190/1.1439012](https://doi.org/10.1190/1.1439012).
- Norio, T., T. Yamaguchi, and G. Zyvoloski, 2008, The Hijiori hot dry rock test site, Japan evaluation and optimization of heat extraction from a two-layered reservoir: *Geothermics*, **37**, no. 1, 19–52, doi: [10.1016/j.geothermics.2007.11.002](https://doi.org/10.1016/j.geothermics.2007.11.002).
- Pettitt, W. S., and R. P. Young, 2007, InSite seismic processor: User operations manual version 2.14: Applied Seismology Consultants Ltd.
- Potluri, N., D. Zhu, and A. D. Hill, 2005, Effect of natural fractures on hydraulic fracture propagation: Presented at the European Formation Damage Conference, SPE.
- Potyondy, D., and J. Autio, 2001, Bonded-particle simulations of the in-situ failure test at Olkiluoto: *Proceedings of 38th U.S. Rock Mechanics Symposium*.
- Potyondy, D., and P. A. Cundall, 2004, A bonded-particle model for rock: *International Journal of Rock Mechanics and Mining Sciences & Geomechanics Abstracts*, **41**, no. 8, 1329–1364, doi: [10.1016/j.ijrmms.2004.09.011](https://doi.org/10.1016/j.ijrmms.2004.09.011).
- Ramakrishnan, H., G. Waters, E. C. Boratko, A. S. Latifzai, and D. Bentley, 2009, Application of downhole injection stress testing in the Barnett shale formation: Presented at the Annual Technical Conference and Exhibition, SPE.
- Rodgerson, J. L., 2000, Impact of natural fractures in hydraulic fracturing of tight gas sands: Presented at the Permian Basin Oil and Gas Recovery Conference, SPE.
- Rutledge, J. T., and W. S. Phillips, 2003, Hydraulic stimulation of natural fractures as revealed by induced microearthquakes, Carthage Cotton Valley gas field, east Texas: *Geophysics*, **68**, no. 2, 441–452, doi: [10.1190/1.1567212](https://doi.org/10.1190/1.1567212).
- Sharma, M. M., P. B. Gadde, R. Sullivan, R. Sigal, R. Fielder, D. Copeland, L. Griffin, and L. Weijers, 2004, Slick water and hybrid fracs in the Bossier: Some lessons learnt: Presented at the Annual Technical Conference and Exhibition, SPE.
- Šílený, J., D. P. Hill, L. Eisner, and F. H. Cornet, 2009, Non-double-couple mechanisms of microearthquakes induced by hydraulic fracturing: *Journal of Geophysical Research*, **114**, B08307, doi: [10.1029/2008JB005987](https://doi.org/10.1029/2008JB005987).
- Vinod, P. S., M. L. Flindt, R. J. Card, and J. P. Mitchell, 1997, Dynamic fluid-loss studies in low-permeability formations with natural fractures: Presented at the Production Operations Symposium, SPE.
- Wanne, T. S., and R. P. Young, 2008, Bonded-particle modeling of thermally fractured granite: *International Journal of Rock Mechanics and Mining Sciences & Geomechanics Abstracts*, **45**, no. 5, 789–799, doi: [10.1016/j.ijrmms.2007.09.004](https://doi.org/10.1016/j.ijrmms.2007.09.004).
- Warpinski, N. R., 1991, Hydraulic fracturing in tight, fissured media: *Journal of Petroleum Technology*, **43**, 146–152, doi: [10.2118/20154-PA](https://doi.org/10.2118/20154-PA).
- Warpinski, N. R., and L. W. Teufel, 1987, Influence of geologic discontinuities on hydraulic fracture propagation: *Journal of Petroleum Technology*, **39**, 209–220, doi: [10.2118/13224-PA](https://doi.org/10.2118/13224-PA).
- White, D., 2009, Monitoring CO₂ storage during EOR at the Weyburn-Midale Field: *The Leading Edge*, **28**, 838–842, doi: [10.1190/1.3167786](https://doi.org/10.1190/1.3167786).
- Young, R. P., and C. Baker, 2001, Microseismic investigation of rock fracture and its application in rock and petroleum engineering: *International Journal of Rock Mechanics*, **7**, 19–27.
- Zhao, X. P., D. Collins, and R. P. Young, 2010, Gaussian-beam polarization-based location method by S-wave for hydraulic fracturing induced seismicity: *Canadian Society of Exploration Geophysicists Recorder*, **35**, 28–33.
- Zhao, X. P., and R. P. Young, 2009, Numerical simulation of seismicity induced by hydraulic fracturing in naturally fractured reservoirs: Presented at the Annual Technical Conference and Exhibition, SPE.
- Zhou, J., M. Chen, Y. Jin, and G. Zhang, 2008, Analysis of fracture propagation behavior and fracture geometry using a tri-axial fracturing system in naturally fractured reservoirs: *International Journal of Rock Mechanics and Mining Sciences & Geomechanics Abstracts*, **45**, no. 7, 1143–1152, doi: [10.1016/j.ijrmms.2008.01.001](https://doi.org/10.1016/j.ijrmms.2008.01.001).